Large-Eddy Simulation of a Normal Shock/Turbulent-Boundary-Layer Interaction in a Dual Passage Test Section

Peter Gioia* and Danesh Tafti†
Department of Mechanical Engineering, Virginia Tech, Blacksburg, VA, 24061

Features of a normal shock-turbulent boundary layer interaction at Mach 1.54 are examined using large-eddy simulation. The geometry used consists of an internal passage divided into an upper unchoked and lower choked section by a shock-holding plate. This geometry and incoming Mach number produces a nearly normal shock and lambda-foot structure on the lower wall leading to separation in the incoming, Re_θ = 1555, turbulent boundary layer. The shock structure is slightly detached from the leading edge of the shock-holding plate and exhibits unsteady but statistically stationary oscillations in the streamwise direction. The turbulent boundary layer upstream of the interaction is first analyzed to verify it is in an equilibrium state. Unsteady and time-averaged quantities are then examined upstream, inside, and downstream of the interaction region. Shock unsteadiness, velocity spectra, and unsteady wall pressure data are analyzed and compared with each other and the upstream turbulent boundary layer to see the effects of the shock/turbulent-boundary-layer interaction.

I. Introduction

Shock/turbulent boundary layer interactions (STBLIs) can have various adverse effects on the performance of aerospace systems, including an increase in drag, loss of lift, increased wall heat flux, and other detrimental impacts on the structure of a vehicle. These effects start in the transonic regime and extend into the hypersonic regime. Within the transonic regime, normal shock waves are present around airfoils, inside over-expanded nozzles, and in engine inlets [1]. In these applications, many factors affect the position of normal shock waves and they are often not stationary, especially when the shock induces boundary layer separation. Experimental and computational efforts have been made to control the position of normal shocks in order to study the underlying physics and reduce their adverse effects on aerospace systems [2, 3].

Normal shock-wave/boundary-layer interactions in transonic and low supersonic flow often exhibit unsteadiness in their position, which is extremely difficult to control experimentally and computationally. This not only makes it challenging for their structure to be studied but also difficult to design structures that can handle the additional unsteady forces induced by the interaction. Various experimental and computational setups, including wall-mounted humps, slots, and porous walls, have been examined in attempts to stabilize a normal shock. Ogawa and Babinsky [4] first proposed a novel wind tunnel setup, which was shown to be able to position a normal shock, making measurements feasible. In its most basic form, the test section is divided into an upper unchoked passage and a lower choked passage by a shock-holding plate. The upper passage cross-sectional area increases around the leading edge of the shock-holding plate. In contrast, the lower passage is of constant area until it reaches a "choking flap" where the cross-sectional area is decreased, choking the flow downstream of the interaction.

This style of setup produces a normal shock that branches into two smaller "feet" which are smeared inside the boundary layer, commonly referred to as a "lambda-foot" (λ-foot) shock structure [1]. This test section configuration has been adopted by Ligrani and Marko [5] and Warning et al. [6], with some nuanced changes. All three setups contain a constant area test section that is divided into an upper unchoked passage and a lower passage choked by a choking flap downstream of the interaction region. The experimental setups differ in how the increase in cross-sectional area is achieved in the upper passage. In the upper passage of [6], the increase in cross-sectional area is achieved with two sharp corners. One is for the beginning of the increase in cross-sectional area, and the other is where the upper passage again becomes a constant area. Ogawa and Babinsky's [4] upper passage does not contain the first sharp corner where the cross sectional area begins to increase, but instead smoothly transitions from the undivided area to the final upper

*Graduate Research Assistant, AIAA Student Member
†William S. Cross Professor, Department of Mechanical Engineering, AIAA Member

passage cross sectional area. The upper passage of Ligrani and Marko [5] removes both sharp corners in the upper passage and smoothly contours the upper wall from the entrance to the outlet of the test section.

Corresponding computational work of this type of configuration has been done using a Reynolds-averaged Navier-Stokes (RANS) approach. Roy et al. used the geometry of [4] and completed computations at Mach 1.3 [7, 8]. The authors did not note any major separation and did not observe shock unsteadiness due to their time-averaged approach. Pizzella et al. also used RANS to examine test section corner effects in this type of setup. In this study, the incoming free-stream velocity was Mach 1.6, and separation of the boundary layer on the lower wall was seen. However, due to the time-averaged computational approach, unsteady phenomena like shock movement are not captured.

The current work aims to examine the geometry of [5] using high-order, time-accurate, large-eddy simulation (LES). Using this approach, we are able to resolve a turbulent shock/boundary-layer interaction with an incoming Mach number of 1.54 in both time and space. Using this geometry and a relatively higher Mach number, a λ-shock structure appears where the front leg separates the incoming turbulent boundary layer along the bottom wall.

II. Numerical Methodology

The LES was performed using FDL3Di, an implicit LES (ILES) solver developed by the AFRL. FDL3Di directly solves the Navier-Stokes in strong conservation form in curvilinear coordinates given in [10] as,

$$\frac{\partial Q}{\partial t}+\frac{\partial F}{\partial \xi}+\frac{\partial G}{\partial \eta}+\frac{\partial H}{\partial \zeta}=\frac{1}{Re}\left(\frac{\partial F_v}{\partial \xi}+\frac{\partial G_v}{\partial \eta}+\frac{\partial H_v}{\partial \zeta}\right), \tag{1}$$

where Q is the solution vector, F, G, H are the inviscid flux vectors and F_v, G_v, H_v are the viscous flux vectors. In curvilinear coordinates these vectors are,

$$Q=\frac{1}{J}\begin{bmatrix}\rho\\ \rho u\\ \rho v\\ \rho w\\ \rho E\end{bmatrix}, F=\frac{1}{J}\begin{bmatrix}\rho U\\ \rho uU+\xi_x p\\ \rho vU+\xi_y p\\ \rho wU+\xi_z p\\ \rho EU+\xi_{x_i}u_i p\end{bmatrix}, G=\frac{1}{J}\begin{bmatrix}\rho V\\ \rho uV+\eta_x p\\ \rho vV+\eta_y p\\ \rho wV+\eta_z p\\ \rho EV+\eta_{x_i}u_i p\end{bmatrix}, \quad H=\frac{1}{J}\begin{bmatrix}\rho W\\ \rho uW+\zeta_x p\\ \rho vW+\zeta_y p\\ \rho wW+\zeta_z p\\ \rho EW+\zeta_{x_i}u_i p\end{bmatrix} \tag{2}$$

$$F_v=\frac{1}{J}\begin{bmatrix}0\\ \xi_{x_i}\tau_{i1}\\ \xi_{x_i}\tau_{i2}\\ \xi_{x_i}\tau_{i3}\\ \xi_{x_i}b_i\end{bmatrix}, G_v=\frac{1}{J}\begin{bmatrix}0\\ \eta_{x_i}\tau_{i1}\\ \eta_{x_i}\tau_{i2}\\ \eta_{x_i}\tau_{i3}\\ \eta_{x_i}b_i\end{bmatrix}, H_v=\frac{1}{J}\begin{bmatrix}0\\ \zeta_{x_i}\tau_{i1}\\ \zeta_{x_i}\tau_{i2}\\ \zeta_{x_i}\tau_{i3}\\ \zeta_{x_i}b_i\end{bmatrix} \tag{3}$$

$$U=\xi_t+\xi_{x_i}u_i, \quad V=\eta_t+\eta_{x_i}u_i, \quad W=\zeta_t+\zeta_{x_i}u_i, \tag{4}$$

where J is the transformation Jacobian. The viscous stress tensor and heat flux vector are,

$$\tau_{ij}=\mu\left(\frac{\partial \xi_k}{\partial x_j}\frac{\partial u_i}{\partial \xi_k}+\frac{\partial \xi_k}{\partial x_i}\frac{\partial u_j}{\partial \xi_k}\right)-\frac{2}{3}\mu\delta_{ij}\frac{\partial \xi_l}{\partial x_k}\frac{\partial u_k}{\partial \xi_l} \tag{5}$$

$$b_i=u_j\tau_{ij}+\frac{k}{(\gamma-1)\,\mathrm{Pr}\,M_\infty^2}\frac{\partial \xi_l}{\partial x_i}\frac{\partial T}{\partial \xi_l}, \tag{6}$$

where $\mu, k, \gamma, Pr, M_\infty$ are the viscosity, thermal conductivity, ratio of specific heats, Prandtl number, and freestream Mach number, respectively. Sutherland's law is employed to compute viscosity and a constant Prandtl number of 0.72 was used. A perfect gas with a zero reference is used as an equation of state, giving the total specific energy as,

$$E=\frac{T}{\gamma(\gamma-1)M_\infty^2}+\frac{1}{2}\left(u^2+v^2+w^2\right). \tag{7}$$

Spatial derivatives are computed using 6$^{\text{th}}$ order compact finite difference schemes of [11]. The solution is advanced in time using the 2$^{\text{nd}}$ order implicit approximate factorization of Beam-Warming [12] with an improved diagonalization of [13] . High-order, low-pass Padé -type filters are used to provide dissipation at high wave numbers [14].

III. Computational Setup

A. Geometry

The geometry used for computations employs an internal channel, which is divided into an upper section and a lower choked section. This geometry was introduced by [4]. Further refinement and extension of this configuration was completed by [5]. The main features of the test-section setup are shown in Fig. 1a. Here, the flow enters from the left and is split by a shock-holding plate positioned between the bottom and top walls of the test section. After the flow is divided, the lower section is choked by a ramp downstream of the leading edge of the shock-holding plate, the choking flap. Ligrani and Marko [5] determined the position and structure of the $\lambda-$ foot shock can be controlled by adjusting the choking flap angle, shock-holding plate height, and shock-holding plate depth into the test section.

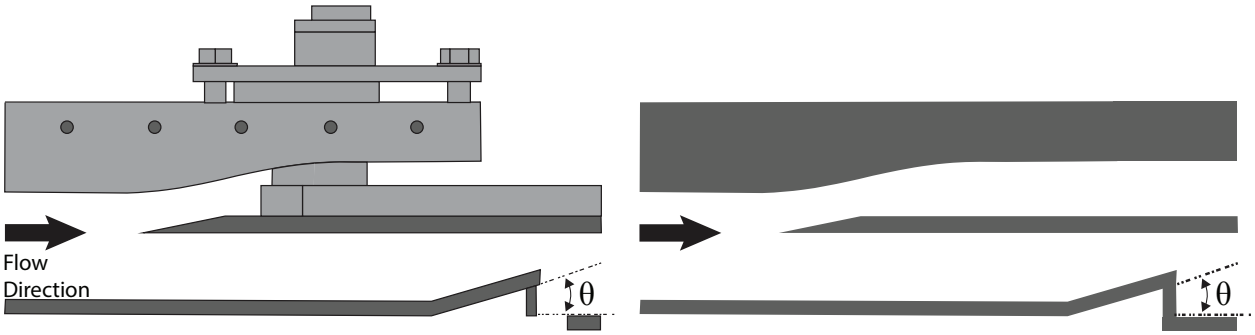

Fig. 1 (a) Schematic of experimental geometry (adapted from [5], with permission from Springer Nature) and (b) simplified computational geometry used.

In order to simplify mesh generation and reduce domain size, the hardware suspending the shock-holding plate was removed, and the choking flap was moved upstream. A basic schematic of the computational geometry is shown in Fig. 1b. The upper wall curvature and shock-holding plate height and depth match that of the optimal configuration determined in [5].

B. Grid & Boundary Conditions

Due to the nature of the internal, dual-passage geometry and the use of curvilinear structured grids in FDL3Di, a multi-grid approach is used for grid generation. The resulting mesh is composed of a system of nine grids with varying levels of refinement. The final system of grids is shown in Fig. 2.

Grids that resolve the incoming turbulent boundary layer (TBL) on the top and bottom walls as well as capture the shock/turbulent boundary-layer interaction in the area around the leading edge of the shock-holding plate are refined, while grids in other areas are coarsened to reduce computational cost. FDL3Di is able to handle an arbitrary set of overset Chimera grids, which do not require point-to-point overlaps between grids [15]. In order to minimize interpolations, point-to-point overlaps are used between grids which resolve the TBL and the region around the shock-holding plate. Upstream of the interaction, grid spacing in the streamwise and spanwise direction is $\Delta x^+ \approx 23$ and $\Delta z^+ \approx 5$, respectively. In the wall normal direction, there are twenty-five points within $y^+ = 10$ with $\Delta y_w^+ \approx 0.5$. The system of grids totaled roughly 249M points. For parallel execution, the system of grids is decomposed into 1792 blocks and run on Virginia Tech's Advanced Research Computing machines [16].

A comparison of simulation and experimental conditions are outlined in Table 1. In order to make the computation practical, the Reynolds number was reduced from approximately 143,000 to about 18,000. This was achieved by maintaining the reference length and velocity but reducing the reference pressure, thereby reducing the reference density and Reynolds number. This approach of reducing the reference pressure while maintaining velocity and length scales has been employed by others [17–19] to maintain scaling consistency between experiments and computations.

A compressible Blasius solution was imposed at the inflow of the domain on the top and bottom walls, which is perturbed using a body-force trip outlined in Section III.C. No-slip, isothermal walls were specified on the top and bottom walls, as well as the shock-holding plate. The wall temperature was specified as $T_w/T_\infty = 1$ on all walls. Periodicity was enforced at the spanwise boundaries. At the exit, the grid was coarsened to prevent spurious reflections,

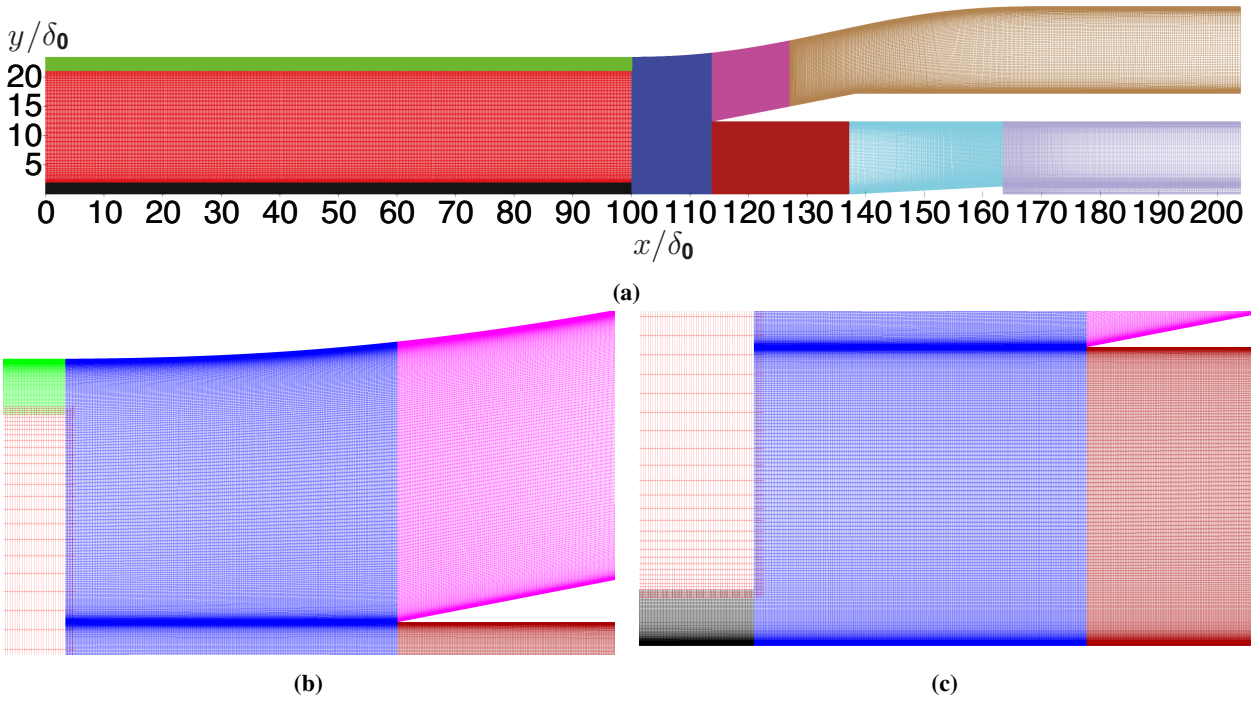

Fig. 2 (a) Overall system of grids and zoomed in locations of the upper (b) and lower (c) channels.

Table 1 Experimental and Simulation Flow Conditions

Property	Experimental	Simulation
M_∞	1.54	1.54
U_∞, m/s	423	423
p_∞, Pa	106, 000	13, 250
T, K	188	188
δ_0, m	3×10^{-3}	3×10^{-3}
Re_{δ_0}	142, 771	17, 776

and all values were extrapolated based on characteristic conditions.

C. Body Force Trip

In order to develop an equilibrium turbulent boundary layer upstream of the interaction region, a counterflow body-force trip is employed of the same form given in [20] to promote transition of the incoming laminar boundary layer. This body force trip source term is based upon a dielectric barrier discharge (DBD) model of [21] but decays exponentially from the origin of the source and allows for application in a chosen direction. The final form of the equation is modeled as

$$f = \frac{2D_c}{\pi \ell_x \ell_y \ell_z} \sin^2\left(\pi \frac{z - Z_0}{\ell_z}\right) \exp\left[-\left(\frac{x - X_0}{\ell_x}\right)^2 - \left(\frac{y - Y_0}{\ell_y}\right)^2\right] \tag{8}$$

where D_c acts like the strength of the trip, l_x, l_y, are the regions of application, and l_z controls the sinusoidal frequency of application in the spanwise direction. The origin of the force is controlled by the coordinates X_0, Y_0, and Z_0. For the present work, the origin was chosen as $X_0 = 2.5\delta_0, Y_0 = 0$, and $Z_0 = 0$. Components of the force were taken as

$$f_x = f\cos(\theta) \qquad f_y = f\sin(\theta) \qquad f_z = 0 \tag{9}$$

which were added to the x, y, and z momentum equations, respectively. The angle, θ, was set to $\theta = 179°$ on the bottom wall, which makes the force act opposite to the incoming flow and nearly parallel. A corresponding term of $f_i u_i$ was added to the energy equation for work. This source term was applied at the top and bottom walls of the domain to generate two turbulent boundary layers in the geometry.

D. Simulation Procedure

The simulation is initialized with freestream conditions throughout the domain and marched in time to a stationary state before time averaging. During the initial transient period, a normal shock wave forms in the lower channel at the downstream edge of the choking flap and moves upstream until it reaches the leading edge of the shock holding plate. Instantaneous contours of velocity at two initial transient times are shown in Fig. 3. Figure 3a shows a time where a shock structure is confined to the lower channel. On the bottom of the lower channel, a λ shock structure with shock induced separation of the boundary layer is seen. On the bottom of the shock holding plate, the shock does not bifurcate into two λ feet, but impinges on the laminar boundary layer which has formed. Due to the laminar nature of the boundary layer, the length of upstream influence is much larger than on the bottom wall of the test section, which allows compression waves upstream of the shock to separate the boundary layer.

Once the shock structure has reached the leading edge of the shock holding plate, it connects with the oblique shock wave attached to the shock holding plate in the upper channel, pictured in Fig. 3b. Upon connecting, the desired λ shock structure forms upstream of the leading edge of the shock holding plate. This initial transient period, from initialization to the formation of the λ shock structure, takes approximately 1750 non-dimensional time units defined as $\tau = tU_\infty/\delta_0$.

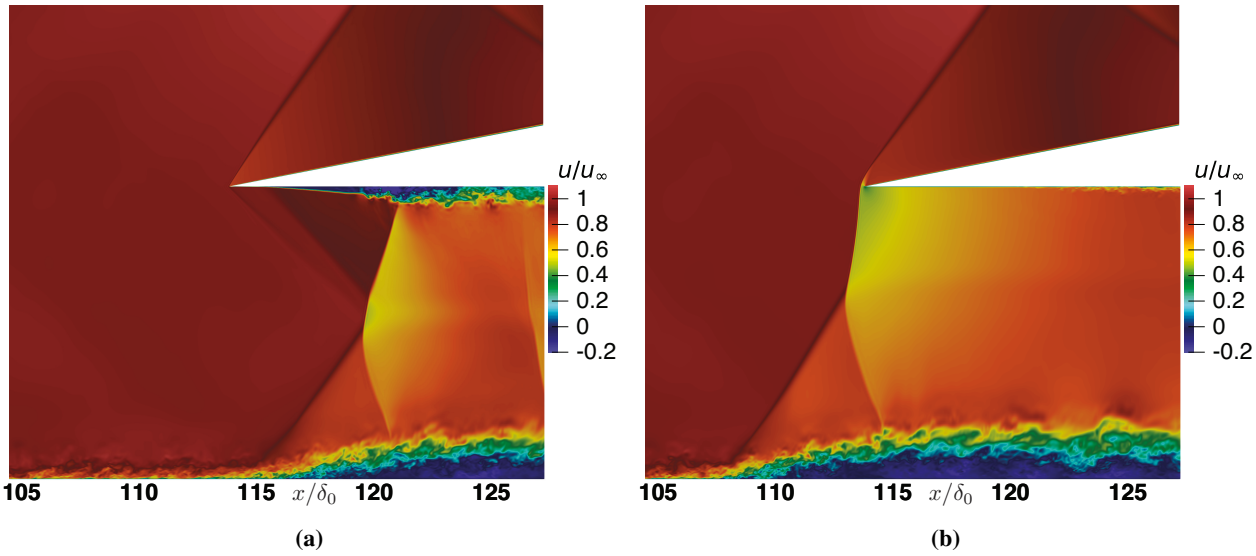

Fig. 3 Instantaneous velocity contours of (a) transient shock traveling upstream in the lower channel, and (b) lower channel shock immediately after passing the leading edge of the shock holding plate.

Once the λ structure has formed, it is allowed to run for approximately three complete oscillations of the main stem, corresponding to ~ 2500 time units, before beginning time averaging. The entire flowfield is averaged for $11,250$ time units to obtain a three dimensional averaged flowfield. The three dimensional flowfield is then averaged in the spanwise direction to obtain a final two-dimensional flowfield for analysis in Sections IV.A and IV.B.

IV. Results & Discussion

A typical instantaneous view of the STBLI is shown in Fig. 4. A nearly normal shock forms just upstream of the leading edge of the shock-holding plate. This shock splits into two feet extending towards the turbulent boundary layer on the bottom wall, ending at the sonic line within the boundary layer. Along the bottom wall, the strong adverse pressure gradient induced by the leading foot of the λ shock structure leads to boundary layer separation and a sharp increase in boundary layer thickness. This sharp boundary layer growth, as well as the large separation region, are qualitatively consistent with the RANS computations of [9], who use a dual passage test configuration at $M_\infty = 1.6$.

Additionally, behind the front leg of the structure is the presence of a small, intermittent, compression wave, seen more clearly in Fig. 4a. The position of the entire shock structure and its parts, as well as the vertical position of the triple point, exhibit unsteady but stationary behavior. Further analyses of their behavior is discussed in Section IV.C.

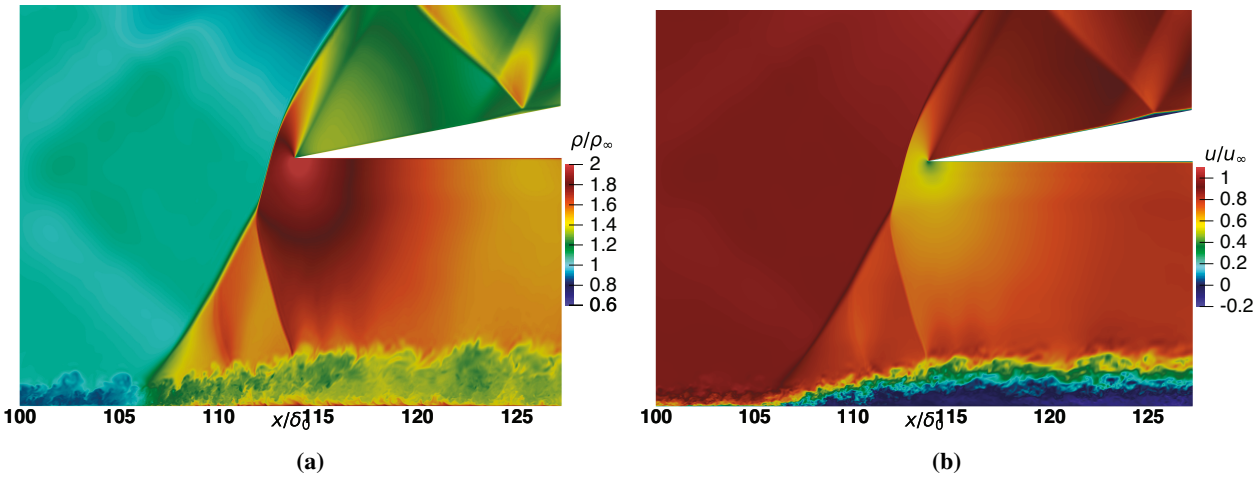

Fig. 4 Instantaneous contours of (a) density and (b) streamwise velocity, normalized by their freestream values.

An isometric view of the interaction including both the upper and lower passages is shown in Fig. 5. Isosurfaces of the Q-criterion show coherent vortical structures in the turbulent boundary layers on the top and bottom walls. The λ-shock structure is visualized by plotting isosurfaces of $|\vec{u} \cdot \nabla p|$. Starting from the triple point and moving upward, the shock turns, becoming oblique and impinging on the upper wall. In this interaction, the boundary layer has a small region of weak separation. After impinging on the upper wall, the shock reflects back onto the shock holding plate and continues downstream in the upper channel. At the bottom wall, between the front and rear legs of the λ structure, the separated boundary layer undergoes a rapid growth in length scales as gauged by the enlargement of coherent vortical structures, especially near the edge of the boundary layer. Downstream of the rear leg, the structures continue to grow.

A. Characteristics of Incoming Turbulent-Boundary-Layer

The turbulent boundary layer upstream of the front lambda-foot is examined to ensure an equilibrium state has been reached before reaching the interaction region. Upstream of the interaction at $x/\delta_0 = 101.5$, the Reynolds number based on momentum thickness and wall viscosity is $Re_\theta = 1555$. Supersonic flat plate DNS results of Pirozzoli and Bernardini with a grid resolution of $\Delta x^+ \sim 5.9$, $\Delta y_w^+ \sim 0.7$, and $\Delta z^+ \sim 5$, are compared against to determine the state of development of the incoming turbulent boundary layer. The DNS case has a freestream velocity of $M_\infty = 2$, and a $Re_\theta = 1327$. The current LES Reynolds stresses at $x/\delta_0 = 101.5$, and these DNS results are plotted in Fig. 6a. The LES results reproduce the DNS [22] profiles quite well with some discrepancies in the peak magnitudes. While the peak of streamwise velocity fluctuations is over predicted, the cross-stream, spanwise and shear stress peaks are slightly under predicted by the LES.

The van Driest transformed velocity profile near the wall is shown in Fig. 6b. The LES results compare well in the viscous sublayer but again, overshoot DNS results in the logarithmic region. This overshoot is also seen in the supersonic flat plate LES of Schwartz and Garmann [23] . In this LES, turbulence generation methods and the effect of the low pass filter coefficient α, which controls dissipation in this ILES framework, is studied for a flat plate at $M_\infty = 1.5$ and $Re_\theta = 1400$. When the authors use $\alpha = 0.4$, the same used in the current simulation, the logarithmic region is over predicted in a similar fashion to the current results.

Lastly, the boundary layer profile upstream of the interaction, at $x/\delta_0 = 101.5$, is compared to the fully developed TBL profile of the fully resolved grid ($\Delta x_i^+ \leq 1$ everywhere) in the DNS of [20]. This DNS has a higher freestream velocity of $M_\infty = 2.3$, and a higher $Re_\theta = 2000$. Figure 7 plots the DNS and LES velocity boundary layer profiles. The LES profile is less full than DNS results around $y/\delta \sim 0.25$, but is in better agreement above $y/\delta_0 \sim 0.55$.

These discrepancies in mean and turbulent flow quantities could be a result of the boundary layer still being in a transitional state spatially with the turbulence not yet fully-developed or could also be due to the LES grid resolution. Additionally, the use of $\alpha = 0.4$ in the low pass filter scheme also likely contributes to overshoot in the logarithmic region

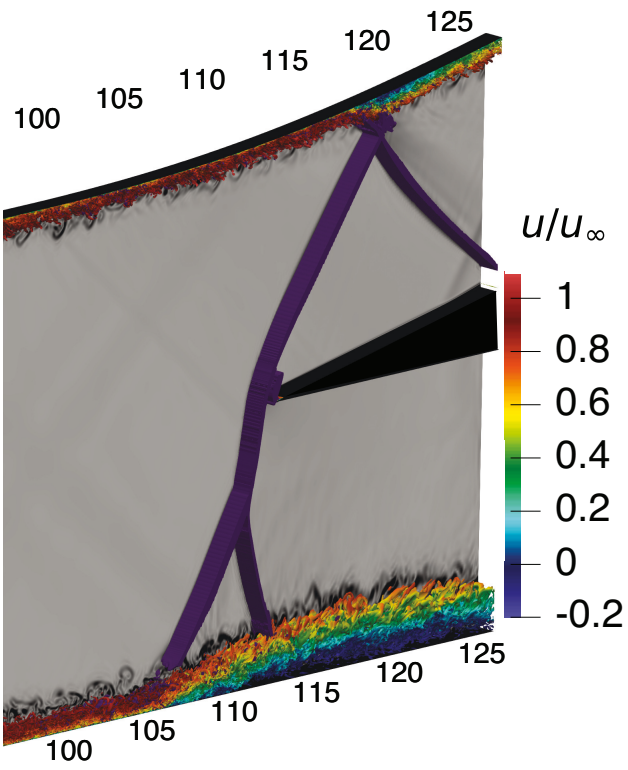

Fig. 5 Instantaneous snapshot of STBLI with isosurface of the Q-criterion on the top and bottom walls colored by streamwise velocity. Structure of λ-foot shock is indicated by isosurfaces of $|\vec{u} \cdot \nabla p|$. Background is colored by density gradient.

of the near wall velocity profile. In spite of these differences compared to DNS, the results are highly representative of a turbulent boundary layer and are deemed to be sufficiently accurate to perform analysis on the normal STBLI created by the dual passage configuration.

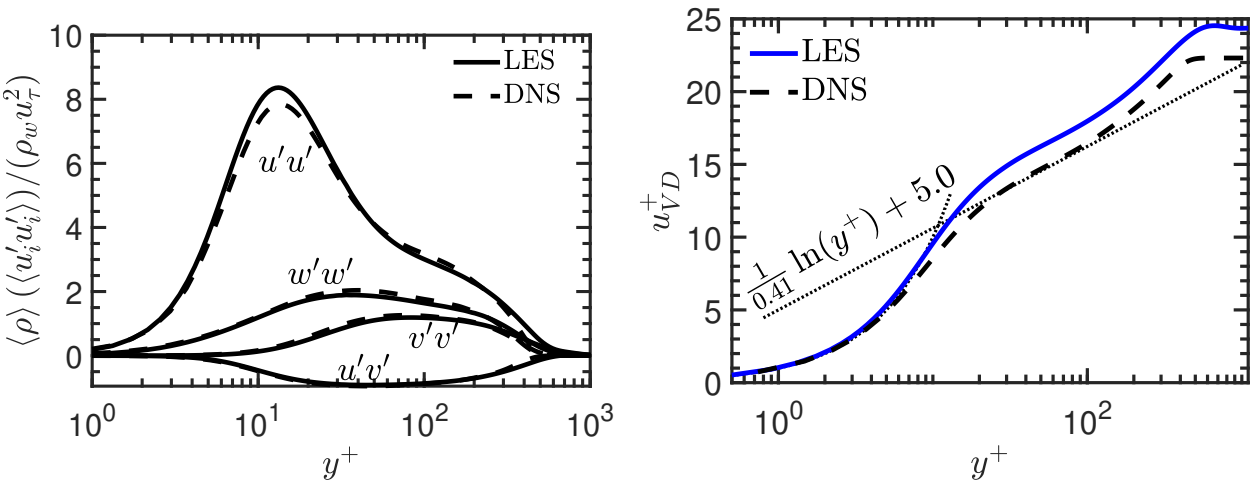

Fig. 6 (a) Reynolds stresses and (b) van Driest transformed [24] turblent boundary layer at $x/\delta_0 = 101.5$. Both plotted with DNS data from [22].

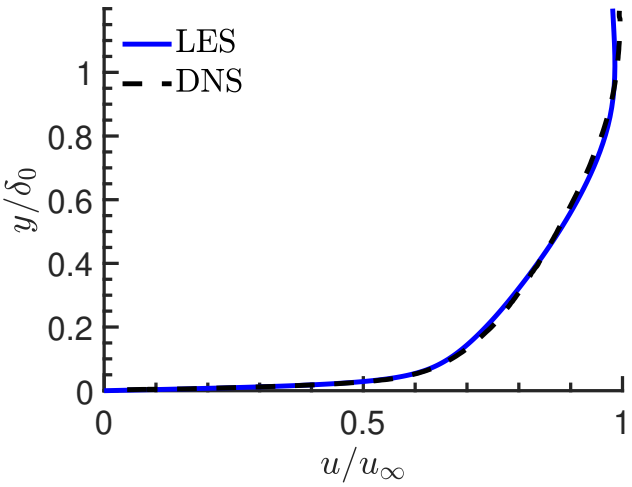

Fig. 7 Time-averaged boundary layer profile upstream of the interaction at $x/\delta_0 = 101.5$, plotted with DNS data from [20].

B. Mean Flow Analysis

Time-averaged contours of density and streamwise velocity are shown in Fig. 8. In both cases, the nearly normal shock and λ-foot structure are easily discernible between the bottom wall of the channel and the shock-holding plate. The relative thickness of these shocks is greater than that observed in the instantaneous contours in Fig. 4 due to the unsteady oscillations of the shock structure.

Under the current state of the incoming turbulent boundary layer, angle of the choking flap, and shock-holding plate position, the shock is detached slightly from the leading edge of the shock-holding plate. Regions of higher density and lower velocity are observed behind the near-normal shock and in front of the leading edge of the shock-holding plate. This can be attributed to not only the presence of the shock but to the stagnation conditions at the leading edge of the shock-holding plate. The strong gradients of density and velocity become weaker as the single main shock splits into two weaker branches.

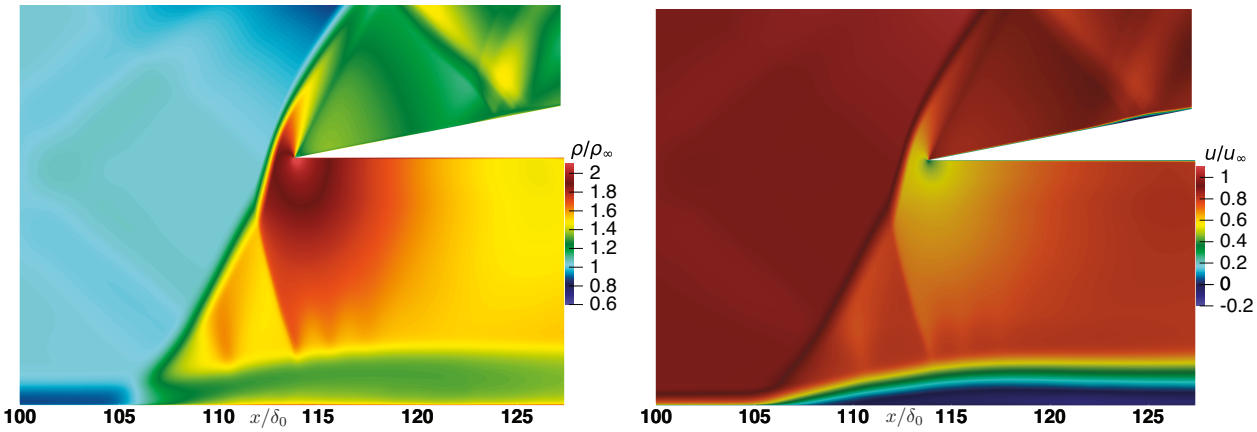

Fig. 8 Time-averaged contours of (a) density and (b) streamwise velocity, normalized by their freestream values.

More closely examining the velocity contour, Fig. 8b, significant growth in the boundary layer thickness at $x/\delta_0 \sim 106$ is observed as it traverses the front leg. Soon after, the boundary layer separates from the strong adverse pressure gradient imposed by the front leg of the shock. The mean separation location is approximately $x/\delta_0 = 108.8$. A contour of local Mach number is shown in Fig. 9. Locally subsonic flow is highlighted by a dark shading in Fig. 9b. A large region of subsonic flow is present behind the main shock which extends almost to the bottom of the rear leg. In

between the bottom of this region and the sonic line of the boundary layer, there is a small region where the flow remains supersonic even as it traverses the rear leg of the shock. Behind the shaded subsonic region, the flow re-accelerates to just above sonic conditions. The flow then remains slightly above or below sonic as it continues throughout the lower channel.

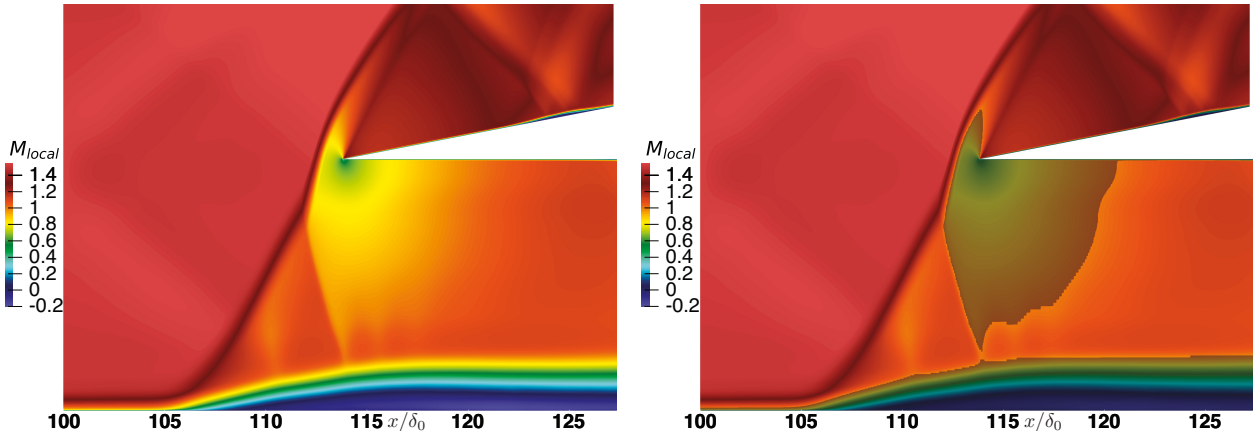

Fig. 9 (a) Contour of local Mach number in the interaction region, and (b) contour with shading to denote regions of locally subsonic flow.

The time-averaged wall pressure profile is plotted in Fig. 10. In the beginning of the interaction zone, the pressure rises sharply starting at $x/\delta_0 \sim 104$ until it reaches a plateau around $x/\delta_0 \sim 112$. This plateau corresponds with the separation of the boundary layer and extends to $x/\delta_0 \sim 120$. The dashed line in Fig. 10 corresponds with the pressure rise downstream of separation, predicted using free interaction theory. Free interaction theory correlates boundary layer separation with pressure rises across SBLIs and the state of the incoming boundary layer [1, 25]. After the end of the first plateau, another increase in pressure begins and plateaus at $x/\delta_0 \sim 150$. This second rise corresponds with the reattachment of the boundary layer farther downstream as seen in separated SBLIs. This second pressure rise recovers to about the pressure rise at sonic conditions (dot-dash line in Fig 10), corresponding well with our previous observation of the flow re-accelerating and remaining near sonic conditions in the lower channel downstream of the interaction.

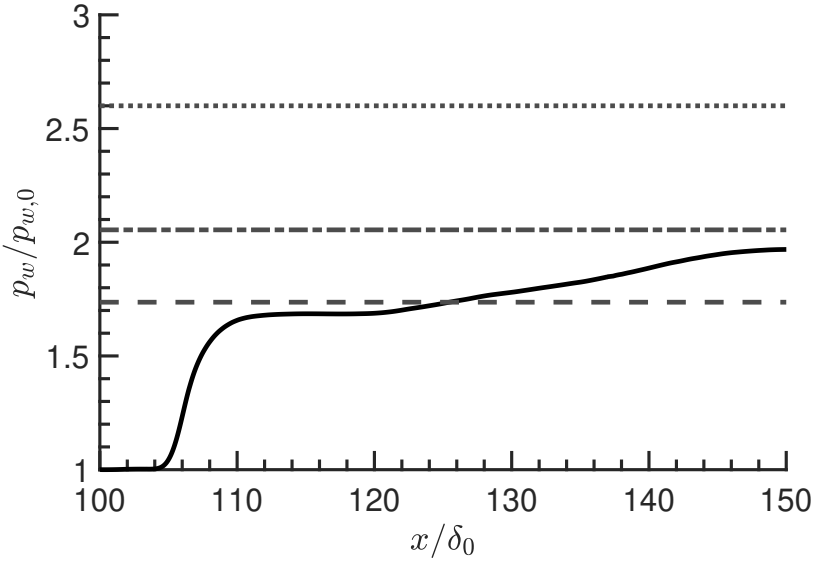

Fig. 10 Time-averaged wall pressure (——), plotted with plateau pressure rise from free interaction theory [25, 26] (- - - -), pressure at sonic conditions (— · —), and inviscid pressure rise (·····) .

Figure 11 shows the streamwise development of skin friction coefficient and boundary layer thickness in the region of interest starting from $x/\delta_0 = 100$. At this location, the skin friction coefficient is 3.2×10^{-3}, which matches well with the value of 3.8×10^{-3} obtained by using the Karman-Schoenherr correlation given in [27] as,

$$C_f = \left[17.09 \left(\log_{10}\left(Re_\theta\right)\right)^2 + 25.11 \left(\log_{10}\left(Re_\theta\right)\right) + 6.012\right]^{-1}. \tag{10}$$

As the boundary layer traverses the front leg of the shock at $x/\delta_0 \sim 104$, there is a sharp drop in its value due to the adverse pressure gradient encountered across the front leg of the shock. The friction coefficient continues to drop, but at a slower rate after the mean location of the front shock leg, until the boundary layer separates at approximately $x/\delta_0 \sim 108.8$. Once the boundary layer separates, the skin friction coefficient remains roughly constant until passing the rear shock leg around $x/\delta_0 = 114$, after which it drops slightly before slowly increasing until reattachment at $x/\delta_0 = 142$. Subjected to the adverse pressure gradient of the shock front leg, the boundary layer thickness exhibits a sharp increase from $x/\delta_0 \sim 106$ until ~ 107.5, where the rate of growth decreases slightly but is still significant.

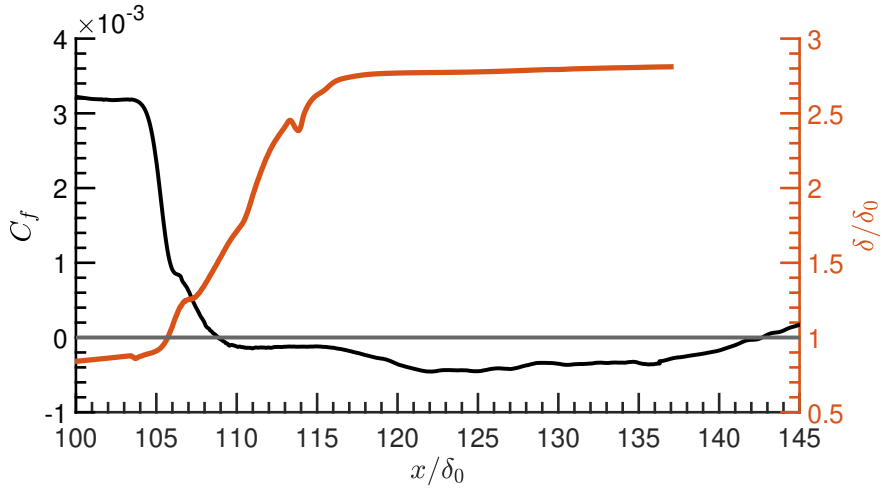

Fig. 11 Skin friction coefficient (Black, Left Axis) and boundary layer thickness (Orange, Right Axis) plotted against streamwise direction.

The boundary layer continues to grow between both shock legs and plateaus after passing the location of the rear leg. Time averaged boundary layer velocity profiles at various streamwise locations are shown in Fig. 12. Upstream of the interaction, the boundary layer is full and has a sharp velocity gradient at the wall, typical of turbulent boundary layers. As it encounters the adverse pressure gradient imposed by the front leg of the shock at $x/\delta_0 = 107.2$, the profile has developed a momentum deficit which increases further in the flow direction. Moving further downstream, the momentum deficit increases in the boundary layer until it can no longer sustain forward momentum at which point it separates at $x/\delta_0 \sim 108.8$. Past the rear leg of the shock structure at $x/\delta_0 = 122.2$, a well-defined recirculating zone with negative flow is established near the wall. Profile recovery is slow and reattachment occurs at $x/\delta_0 = 142$. After reattachment, the boundary layer begins to recover as seen at $x/\delta_0 = 157.9$.

The streamwise pressure profiles at various locations on the main shock are plotted in Fig. 13. Four locations are plotted starting from near the triple point (Loc. A), moving all the way to just under the shock holding plate. All profiles exhibit a sharp but smooth increase in pressure as they move through the shock, then show an additional increase in pressure farther downstream. This second increase in pressure is influenced by the proximity to the shock holding plate. As the locations move towards the plate, the second increase in pressure becomes sharper and larger in magnitude due to the stagnation conditions at the leading edge of the shock holding plate.

Streamwise pressure profiles at locations below the triple point are shown in Fig. 14. A sharp increase in pressure occurs at the front leg but is less than that seen across the main trunk due to the oblique nature of the front leg. A second pressure rise occurs through the rear leg. There is an increasing rise in pressure across the rear leg as the rear shock gets stronger towards the triple point.

The evolution of streamwise normal Reynolds stress is plotted in Fig. 15. In the incident turbulent boundary layer at $x/\delta_0 = 101.54$, the peak value of 0.0126 is observed at $y/\delta_0 = 0.0234$. After the boundary layer traverses the front leg

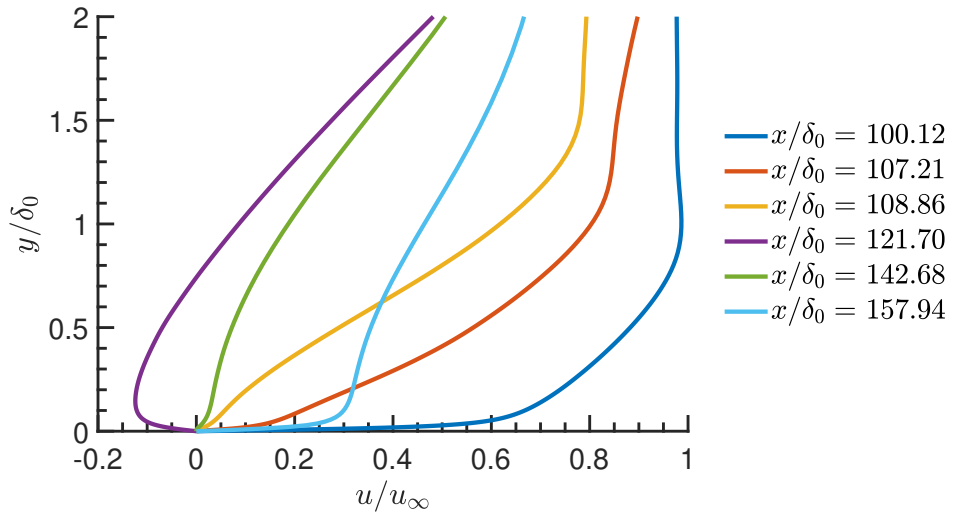

Fig. 12 (a) Streamwise evolution of boundary layer profiles: Upstream (Dark Blue); Separation (Yellow); Fully separated (Purple); and Reattachment (Green).

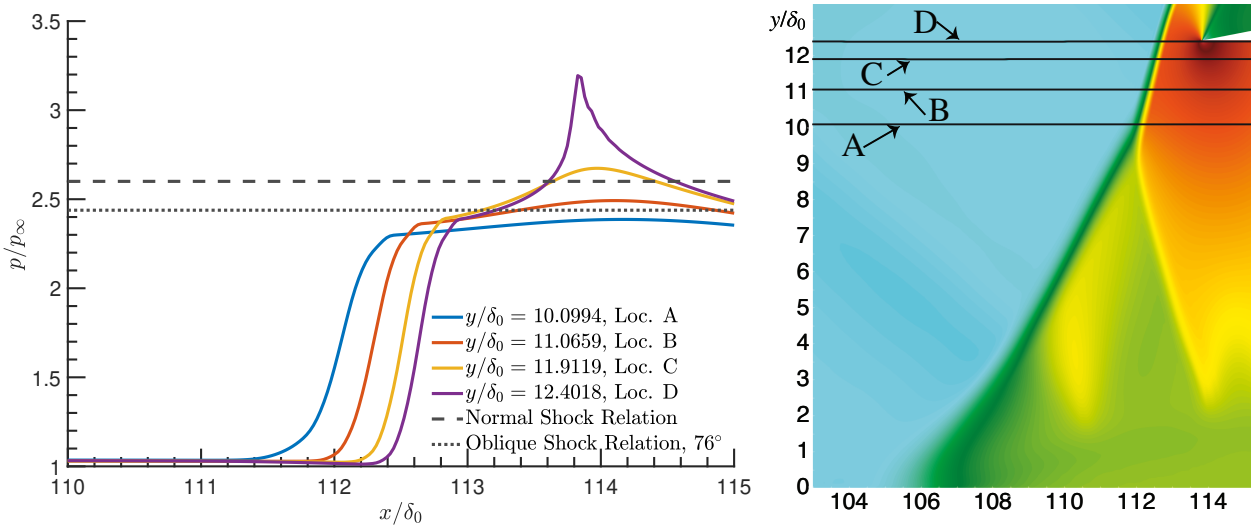

(a) **(b)**

Fig. 13 (a) Time-averaged pressure at different y/δ_0 locations along the main shock; oblique shock static pressure relation at the approximate angle of the main shock (·····), and normal shock relation (- - - -). (b) Locations on main shock where pressure profiles are taken.

of the shock at $x/\delta_0 = 107.21$, it is observed that the stress magnitude increases in the outer part of the boundary layer as does the peak magnitude which increases to 0.0137 and shifts to $y/\delta_0 = 0.238$. Post separation at $x/\delta_0 = 109.9$, the peak magnitude reduces to 0.0117 and shifts further outward to $y/\delta_0 = 0.804$. With each subsequent x-location plotted ($x/\delta_0 = 113.83$ and 120.19), both of which are located in the separated boundary layer, the peak magnitude reduces as the location of the peaks shift to larger y/δ_0 values.

The cross-stream Reynolds stress, plotted in Fig. 16, also sees an increase in peak magnitude after it crosses the front foot of the shock structure. Compared to the incident turbulent boundary, the peak increases from 1.79×10^{-3} to 3.17×10^{-3}. However, the location of the peak magnitude remains approximately the same, only shifting from $y/\delta_0 = 0.153$ to 0.182. After separation, the peak magnitude increases further to 3.83×10^{-3} and shifts to a location of $y/\delta_0 = 0.727$. Further downstream, the peak magnitude locations continue to shift farther towards the edge of the boundary layer and their magnitudes decrease slightly back to 3.13×10^{-3} and 2.84×10^{-3}, but are still higher than that

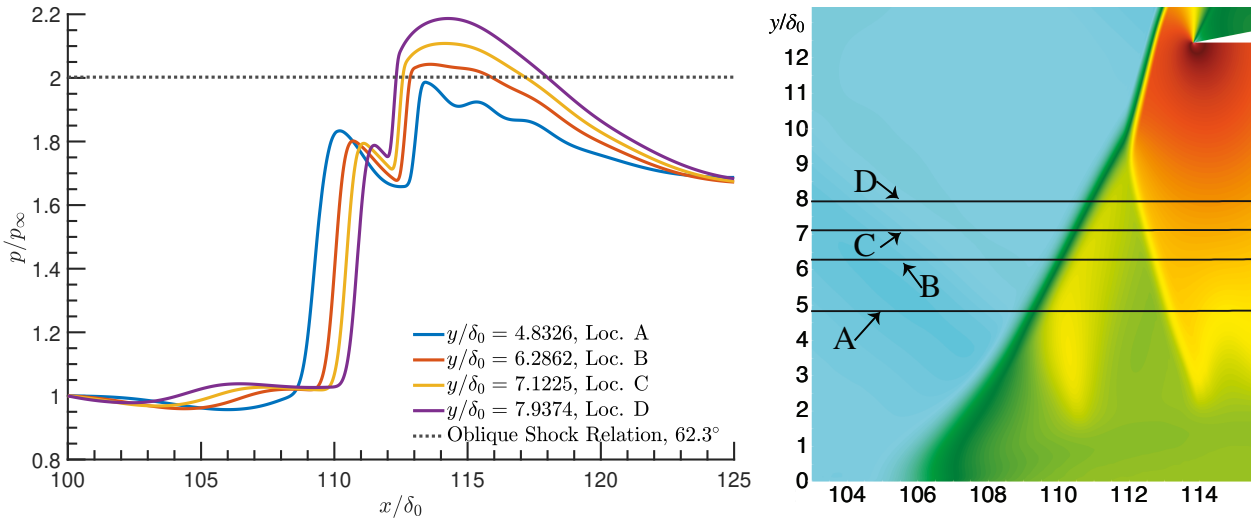

(a) **(b)**

Fig. 14 Time-averaged pressure across front and rear λ legs at different y/δ_0 locations; oblique shock static pressure relation at the approximate angle of the front leg (·····).

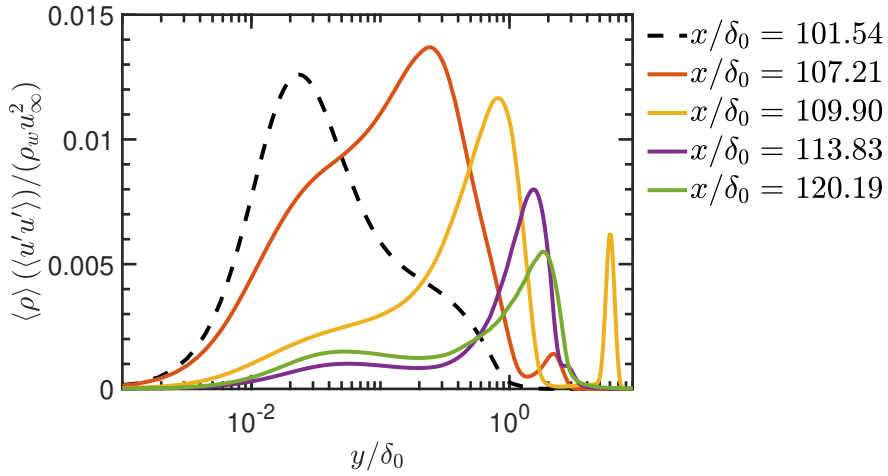

Fig. 15 Streamwise normal Reynolds stress profiles spatially evolving in the streamwise direction.

of the incident turbulent boundary layer.

The Reynolds shear stresses see a similar behavior to the streamwise and cross-stream normal stresses. Plotted in Fig. 17, the peak shear stress increases when the flow traverses the front foot. Additionally, a secondary peak is seen at $y/\delta_0 = 2.208$. After separation, the peak magnitude reduces to -1.726×10^{-3} and moves farther out of the boundary layer to $y/\delta_0 = 0.727$. Here, a shear layer is formed at $y/\delta_0 = 5.953$ which has a large peak at -3.21×10^{-3}. In the separated region, the magnitudes of the peak remain approximately the same while shifting slightly farther out into the boundary layer at $y/\delta_0 = 1.807$.

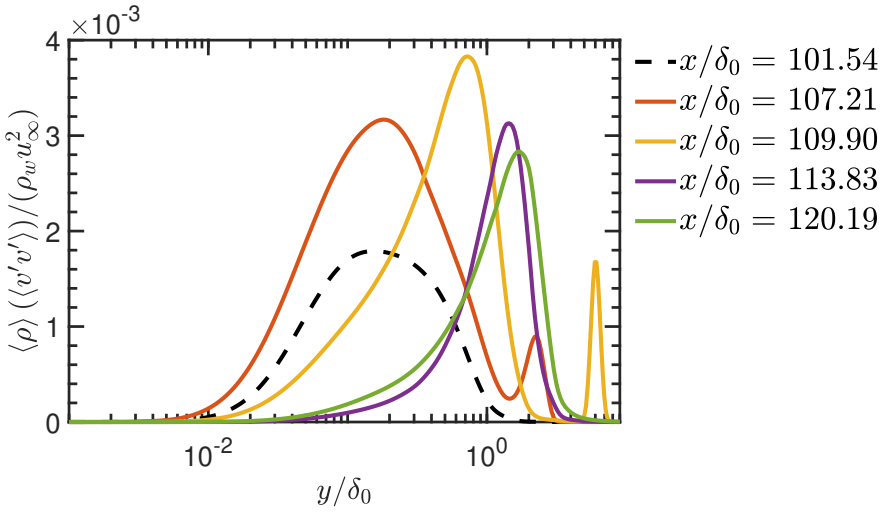

Fig. 16 Wall normal Reynolds stress profiles spatially evolving in the streamwise direction.

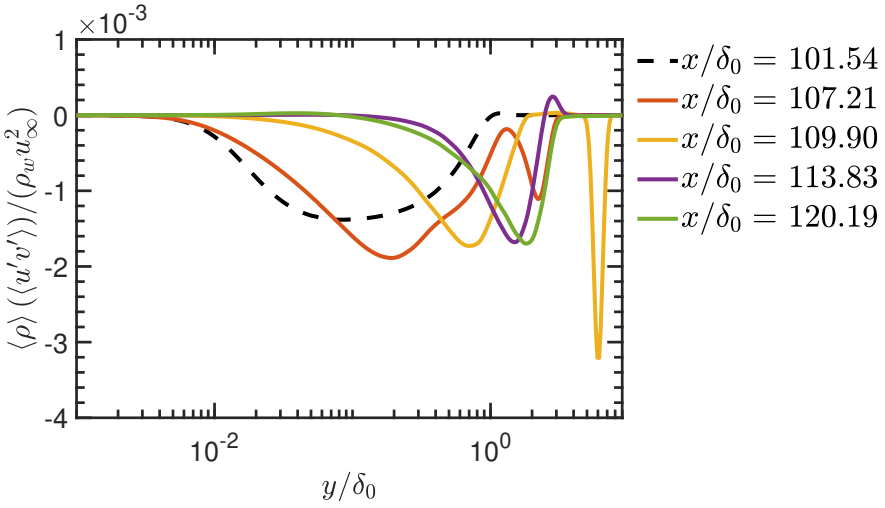

Fig. 17 Reynolds shear stress profiles spatially evolving in the streamwise direction.

C. Frequency Analysis

Turbulent SBLIs with separation often exhibit a low-frequency unsteadiness, whose origin is not yet fully understood [28]. Here, the unsteady nature of the λ-shock structure and its relation to unsteady wall pressure fluctuations is investigated. Shock tracking is employed by sampling pressure values along the red, blue, and green lines in the streamwise direction shown in Fig. 18 . While the red line tracks the main stem of the shock, the blue and green locations track the front and back leg of the lambda foot, respectively, near the edge of the boundary layer. A fifth order WENO switch is used along these lines to identify the unsteady location of the shock. The switch is given in [29] as,

$$\phi_i = \left[c_1(p_{i+1} - p_{i-1})^2 + c_2(p_{i+1} - 2p_i + p_{i-1})^2\right]^{c_3} \tag{11}$$

with $c_1 = 1/4, c_2 = 13/12$, and $c_3 = 2$. This switch is applied in the streamwise direction along the red, blue, and green lines in Fig. 18 and the location is determined by the maxium value of the switch.

The raw fluctuating shock signal and corresponding normalized premultiplied power spectral density (PSD) for the main shock is plotted in Fig. 19. The PSD is computed using Welch's method [30], using eight segments and a 50% overlap window. The PSD is then premultiplied by its corresponding Strouhal number and normalized as,

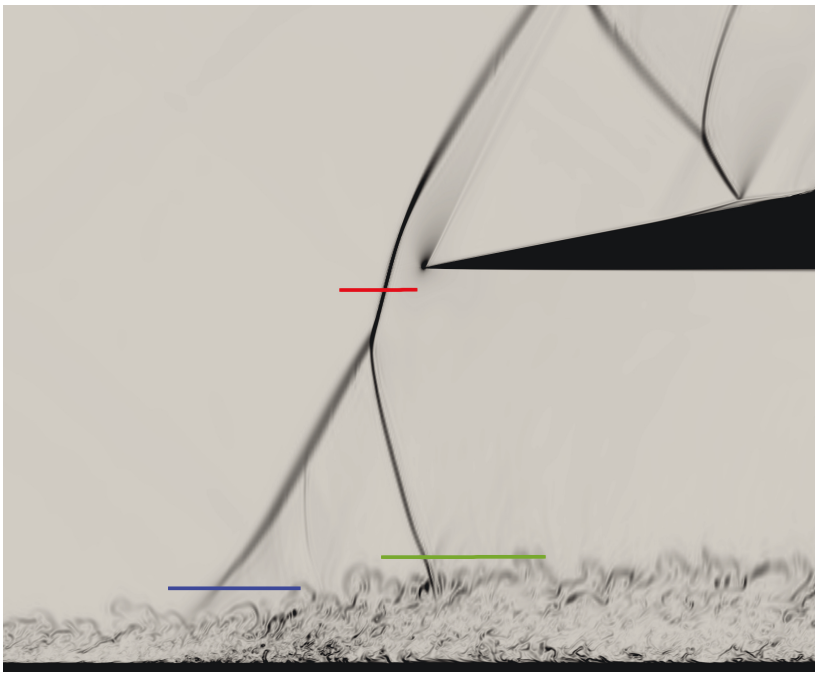

Fig. 18 Instantaneous pseudo-Schlieren contour of the interaction. Shock tracking is utilized along the red, blue, and green lines to track the location of the main shock, front leg, and rear leg,respectively.

$$(\text{Normalized PSD})_i = \frac{(St_L)_i (PSD)_i}{\sum_{i=1}^{n_i} (St_L)_i (PSD)_i}. \tag{12}$$

Using this form makes for easier comparisons of PSDs where the total energy content may differ. The length scale used in the Strouhal number, $L_{int} = 6.3$ mm, is the maximum displacement of the front leg location. The displacement of the of the front leg is chosen to be the length scale as the front shock directly interacts and separates the incoming turbulent boundary layer. The PSD of the main shock location has two distinct peaks at Strouhal numbers of 2.56×10^{-3} and 8.96×10^{-3}. These Strouhal numbers are the same as the peak frequencies observed for the front leg, plotted in Fig. 20. However, the relative strength of fluctuations at St = 2.56e-3 is greater in the main shock than in the front leg. In the main shock, the energy at this Strouhal number makes up about 12% of the total PSD, while in the front leg it makes up about 2.8% of the total PSD. The front leg PSD contains higher relative amounts of energy at the higher Strouhal numbers. This difference in energy distribution is likely due to the influence of fluctuations in the turbulent boundary layer near where the front foot location is being measured, causing additional energy to be distributed to higher frequencies.

The rear leg location, plotted in Fig. 21, exhibits unsteadiness at higher Strouhal numbers than both the front leg and main shock. The PSD of the rear leg location contains multiple peak frequencies and the overall distribution of energy is more broadband when compared to the front leg and main shock. While the distribution has a larger spread, there are still two "groups" of peaks which correspond with $St_L = 9.39 \times 10^{-3}$ and $St_L = 1.58 \times 10^{-2}$. Similar to that of the front leg, the rear leg fluctuations have energy distributed at higher Strouhal numbers influenced by the proximity to the turbulent boundary layer.

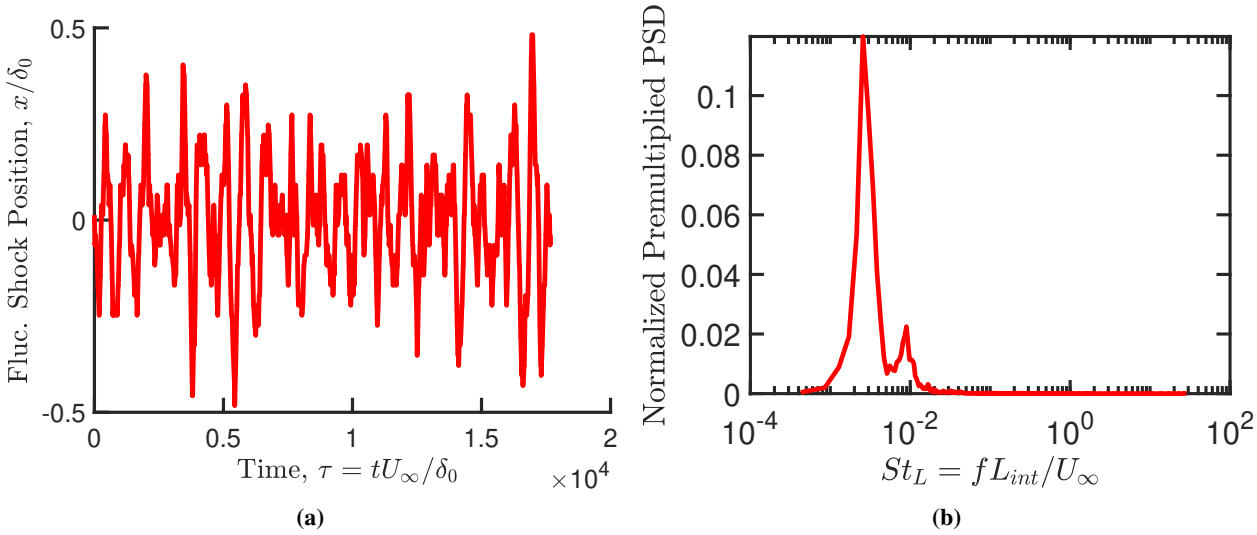

(a) (b)

Fig. 19 (a) Raw fluctuating shock position of the main shock, red line in Fig 18. (b) Premultiplied power spectral density of the fluctuating shock position. Values are normalized such that their sum is unity.

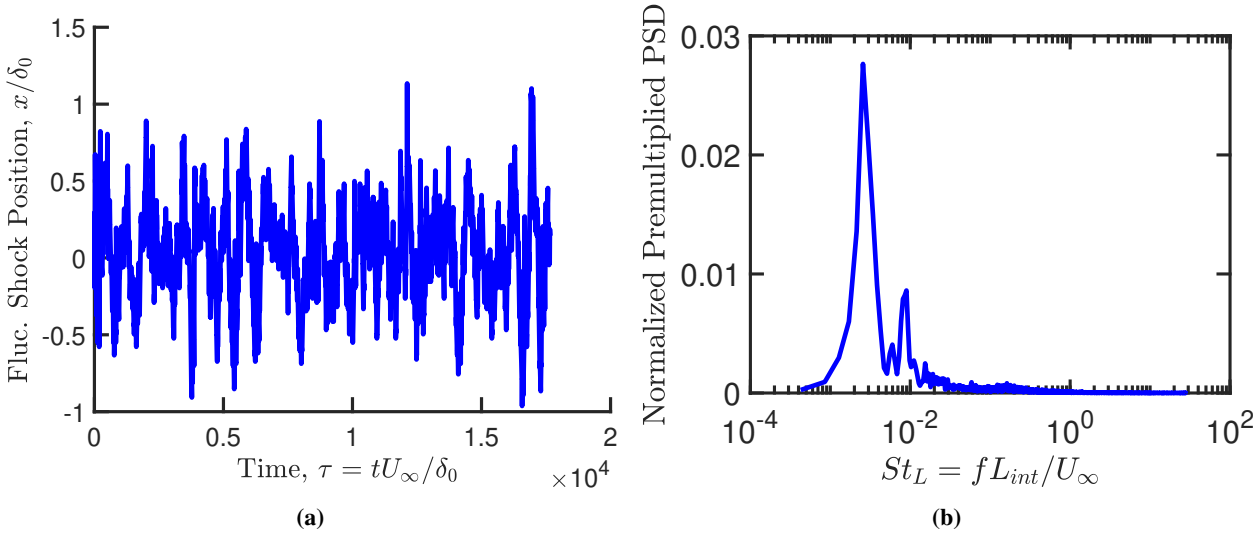

(a) (b)

Fig. 20 (a) Raw fluctuating shock position of the front leg, blue line in Fig 18. (b) Premultiplied power spectral density of the fluctuating shock position. Values are normalized such that their sum is unity.

A contour of weighted PSD of pressure fluctuations at the wall is shown in Fig. 22. Here, the weighted PSD also premultiplies each PSD value with its corresponding Strouhal number, but divides it by the integrated area of the PSD as,

$$(\text{Weighted PSD})_i = \frac{(St_L)_i (PSD)_i}{\int_{St_{L,\text{min}}}^{St_{L,\text{samp}}/2} (PSD) dSt_L}. \tag{13}$$

By premultiplying the PSD at its corresponding Strouhal number, peak regions of energy for that x-location are emphasized in the contour. Before $x/\delta_0 = 104$ upstream of the interaction with the front leg of the shock, the spectral characteristics of wall pressure fluctuations are influenced solely by the turbulent boundary layer and the PSDs exhibits peak amplitudes at $St \sim 2.5$. Beginning at $x/\delta_0 = 104$ until about $x/\delta_0 = 108$, the wall pressure fluctuations carry the most energy at lower Strouhal numbers with peak energy at $St \sim 3\text{e}{-3}$ and $St \sim 9\text{e}{-3}$ which roughly corresponds with the front leg oscillation frequency of $St = 2.58\text{e}{-3}$ and $St = 8.96\text{e}{-3}$.

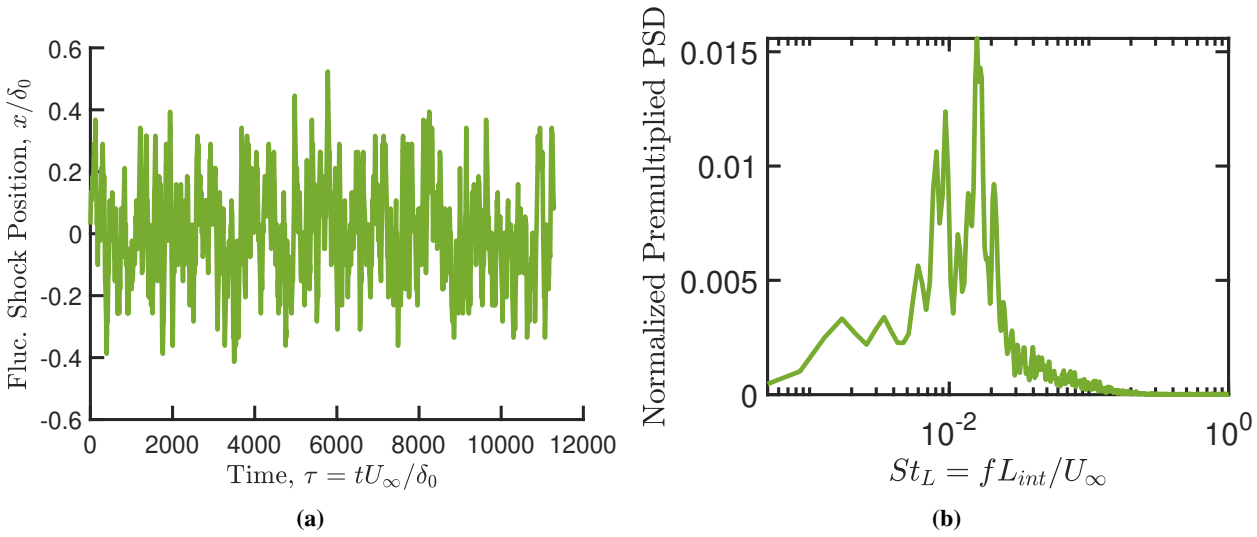

(a) **(b)**

Fig. 21 (a) Raw fluctuating shock position of the rear leg, green line in Fig 18. (b) Premultiplied power spectral density of the fluctuating shock position. Values are normalized such that their sum is unity.

Downstream of $x/\delta_0 = 108$ to $x/\delta_0 = 113$, in the region between the two legs of the shock, wall pressure fluctuations are no longer directly influenced by the unsteadiness of the front shock leg. The energy distribution does not quite recover to that of a canonical turbulent boundary layer, nor does it transition to the peak frequencies characteristic of the back leg unsteadiness. Instead, it shifts to a range of lower frequencies ranging from $St \sim 6e{-}2$ to $St \sim 1$ which lies between the low frequency unsteadiness of the shock and the higher frequency fluctuations in the turbulent boundary layer. There is however a small overlap region where frequencies between the upstream and downstream spectra coincide around $St = 1$. This overlap region decays farther downstream and the peak band of frequencies becomes more distinct between $St \sim 0.1$ to 0.12.

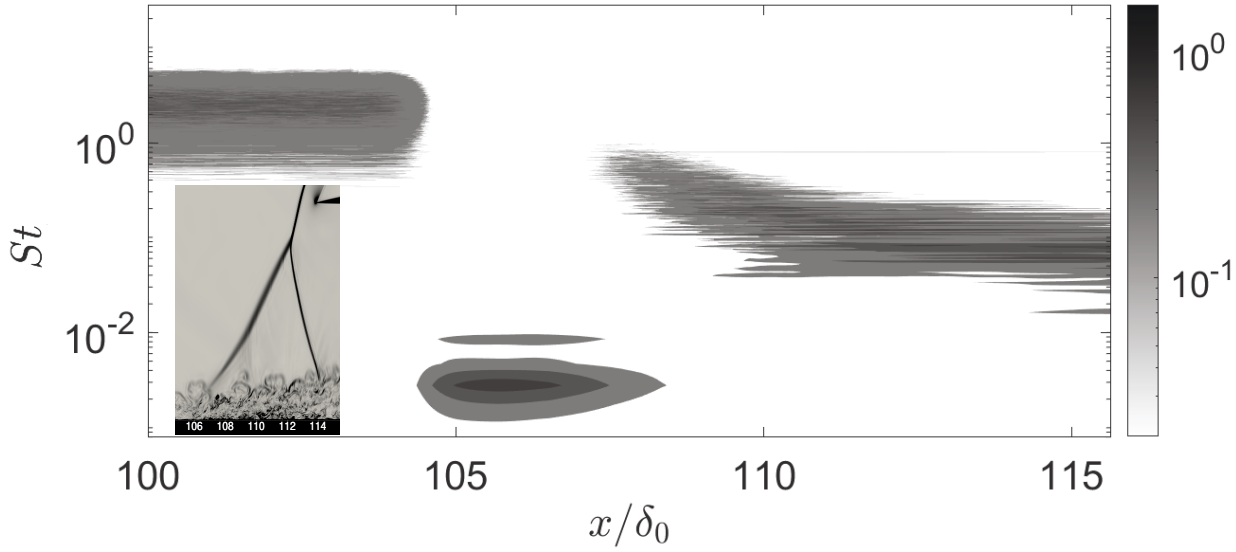

Fig. 22 Weighted PSD of pressure fluctuations at $y/\delta_0 = 0$.

One dimensional velocity spectra at multiple streamwise locations are shown in Fig. 23. All values are normalized by the value at the lowest frequency of the upstream spectrum at $x/\delta_0 = 100.13$. Upstream of the interaction, the spectra exhibits typical behavior of a turbulent boundary layer, following the $-5/3$ law in the inertial subrange. As the boundary layer begins to traverse the front shock foot at $x/\delta_0 = 105.14$, an increase in energy is seen at lower frequencies and

a peak emerges at $St = 2.5 \times 10^{-3}$ which corresponds to the peak front foot oscillation frequency. After traversing the front foot at $x/\delta_0 = 107.11$ there is an increase in energy across all frequencies with the peak at $St = 2.5 \times 10^{-3}$ becoming more distinct. After separation, but still between the front and rear foot, the energy distribution becomes less full at Strouhal numbers greater than 0.13, when compared to the upstream distribution. Farther downstream at $x/\delta_0 = 120.17$, the distribution appears to begin recovering to a canonical profile.

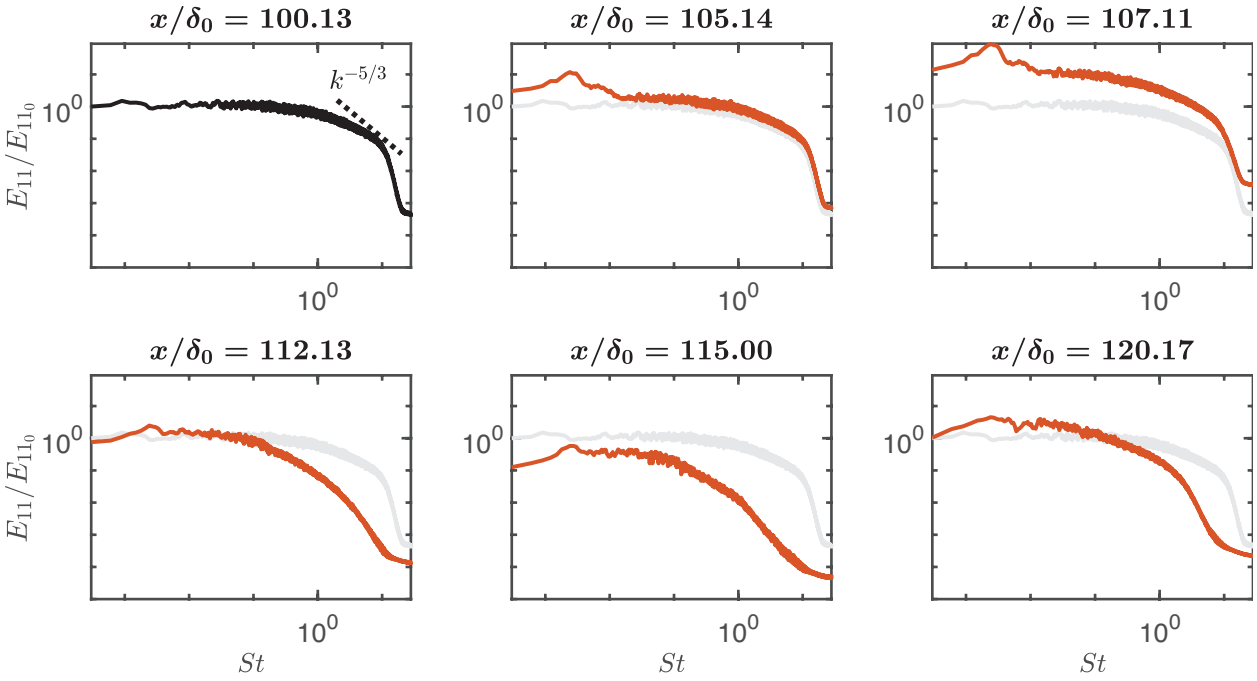

Fig. 23 1D normalized velocity spectra at $y/\delta_0 = 0.26$.

V. Conclusions

High-fidelity LES of a normal STBLI was performed on a dual passage test section. This configuration of test section has not previously been studied using time-accurate computational techniques. Under the current flow conditions and geometry, an unsteady, nearly normal, λ-foot shock structure is produced upstream of the shock-holding plate. The mean structure and flow variables are qualitatively and quantitatively compared to other computational results and theory. Significant boundary layer growth and strong separation of the boundary layer are seen due to the interaction. Additionally, the SBLI leads to an amplification and redistribution of the Reynolds normal and shear stresses. At the beginning of the interaction, all Reynolds stresses see an initial increase in peak magnitude and their location shift away from the wall. Downstream of separation, the location of the peak Reynolds stresses continues to move away from the wall. Cross-stream and shear stresses remain amplified after separation of the boundary layer. Unsteady shock position, wall pressure, and velocity spectra are analyzed and compared against each other and the undisturbed upstream boundary layer. The current configuration and incoming boundary layer produce a shock structure which exhibits a characteristic low frequency of $St = 2.56 \times 10^{-3}$. This characteristic frequency is strongest in the main stem of the shock structure but is also present in the front λ leg. The position of the front and rear λ legs both exhibit additional unsteadiness at higher frequencies than the main stem due to their proximity to the boundary layer. The characteristic low frequency is also seen in fluctuating wall pressure spectra at the location of the front λ foot. After separation, the fluctuating wall pressure spectra does not contain any significant amount of energy at low frequencies but instead is redistributed to an intermediate band of frequencies between the characteristic low frequency and the high frequencies of the upstream turbulent boundary layer.

This work extends previous steady state computations to now examine unsteady dynamics of a normal STBLI using a dual passage test section configuration. Coupling time accurate computational methods with this geometry now allows for additional analysis in areas of unsteady heat transfer, mechanisms of unsteadiness, and experimental comparison, which can contribute to the understanding of shock boundary layer interaction physics.

Acknowledgments

This material is based upon work supported by the National Science Foundation under Grant No. CBET 2041622. The authors acknowledge Advanced Research Computing at Virginia Tech for providing computational resources and technical support that have contributed to the results reported within this paper: https://arc.vt.edu/.The authors would like to acknowledge Dr. Daniel Garmann and Dr. Miguel Visbal at AFRL for their assistance in using FDL3Di, and would also like to thank Dr. Phillip Ligrani for providing experimental setup information and helpful discussions.

References

[1] Babinsky, H., and Harvey, J. (eds.), *Shock Wave-Boundary-Layer Interactions*, Cambridge Aerospace Series, Cambridge University Press, Cambridge ; New York, 2011. URL www.cambridge.org/9780521848527.

[2] Ligrani, P. M., McNabb, E. S., Collopy, H., Anderson, M., and Marko, S. M., "Recent Investigations of Shock Wave Effects and Interactions," *Advances in Aerodynamics*, Vol. 2, No. 1, 2020, p. 4. https://doi.org/10.1186/s42774-020-0028-1, URL https://AIA.Springeropen.com/articles/10.1186/s42774-020-0028-1.

[3] Loth, E., Titchener, N., Babinsky, H., and Povinelli, L., "Canonical Normal Shock Wave/Boundary-Layer Interaction Flows Relevant to External Compression Inlets," *AIAA Journal*, Vol. 51, No. 9, 2013, pp. 2208–2217. https://doi.org/10.2514/1.J052175, URL https://arc.aiaa.org/doi/10.2514/1.J052175.

[4] Ogawa, H., and Babinsky, H., "Wind-Tunnel Setup for Investigations of Normal Shock Wave/Boundary Layer Interaction Control," *AIAA Journal*, Vol. 44, No. 11, 2006, pp. 2803–2805. https://doi.org/10.2514/1.24370, URL https://arc.aiaa.org/doi/10.2514/1.24370.

[5] Ligrani, P. M., and Marko, S. M., "Parametric Study of Wind Tunnel Test Section Configurations for Stabilizing Normal Shock Wave Structure," *Shock Waves*, Vol. 30, No. 1, 2020, pp. 77–90. https://doi.org/10.1007/s00193-019-00911-5, URL http://link.springer.com/10.1007/s00193-019-00911-5.

[6] Warning, S., Lambert, S., McQuilling, M., Mani, M., and Scharnhorst, R., "Shock-Induced Separation and Control in a 4.32-Aspect-Ratio Test Section," *Journal of Propulsion and Power*, Vol. 40, No. 2, 2024, pp. 285–302. https://doi.org/10.2514/1.B39044, URL https://arc.aiaa.org/doi/10.2514/1.B39044.

[7] Roy, S., Sandhu, J. P. S., and Ghosh, S., "Drag Reduction in Transonic Shock-Wave/Boundary-Layer Interaction Using Porous Medium: A Computational Study," *Shock Waves*, Vol. 31, No. 2, 2021, pp. 117–132. https://doi.org/10.1007/s00193-021-01009-7, URL https://link.springer.com/10.1007/s00193-021-01009-7.

[8] Roy, S., Subramaniam, K., and Ghosh, S., "Positioning of Normal Shock in a Novel Constant-Area Test Section: A Numerical Study," *AIAA Journal*, Vol. 57, No. 12, 2019, pp. 5582–5587. https://doi.org/10.2514/1.J057834, URL https://arc.aiaa.org/doi/10.2514/1.J057834.

[9] Pizzella, M., Warning, S., Jennerjohn, M., McQuilling, M., Purkey, A., Scharnhorst, R., and Mani, M., "Shock-Wave/Boundary-Layer Interaction in a Large-Aspect-Ratio Test Section," *AIAA Journal*, Vol. 55, No. 9, 2017, pp. 2919–2928. https://doi.org/10.2514/1.J055592, URL https://arc.aiaa.org/doi/10.2514/1.J055592.

[10] Gaitonde, D. V., and Visbal, M. R., "High-Order Schemes for Navier-Stokes Equations: Algorithm and Implementation Into FDL3DI:," Technical Report, Aug. 1998. https://doi.org/10.21236/ADA364301, URL http://www.dtic.mil/docs/citations/ADA364301.

[11] Lele, S. K., "Compact Finite Difference Schemes with Spectral-like Resolution," *Journal of Computational Physics*, Vol. 103, No. 1, 1992, pp. 16–42. https://doi.org/10.1016/0021-9991(92)90324-R, URL https://linkinghub.elsevier.com/retrieve/pii/002199919290324R.

[12] Beam, R. M., and Warming, R. F., "An Implicit Factored Scheme for the Compressible Navier-Stokes Equations," *AIAA Journal*, Vol. 16, No. 4, 1978, pp. 393–402. https://doi.org/10.2514/3.60901, URL https://arc.aiaa.org/doi/10.2514/3.60901.

[13] Pulliam, T. H., Jespersen, D. C., Bodony, D. J., and Bidadi, S., "Improved Eigenvectors for Pulliam-Chaussee Diagonalized Approximate-Factorization Algorithm," *Journal of Computational Physics*, Vol. 412, 2020, p. 109443. https://doi.org/10.1016/j.jcp.2020.109443, URL https://linkinghub.elsevier.com/retrieve/pii/S0021999120302175.

[14] Gaitonde, D. V., and Visbal, M. R., "Pade-Plusmn;-Type Higher-Order Boundary Filters for the Navier-Stokes Equations," *AIAA Journal*, Vol. 38, No. 11, 2000, pp. 2103–2112. https://doi.org/10.2514/2.872, URL https://arc.aiaa.org/doi/10.2514/2.872.

[15] Morgan, P., Visbal, M., and Rizzetta, D., "A Parallel Overset Grid High-Order Flow Solver for Large Eddy Simulation," *Journal of Scientific Computing*, Vol. 29, No. 2, 2006, pp. 165–200. https://doi.org/10.1007/s10915-005-9011-6, URL http://link.springer.com/10.1007/s10915-005-9011-6.

[16] "Advanced Research Computing at Virginia Tech," , Nov. 2023. URL https://arc.vt.edu/about.html.

[17] Vyas, M. A., Waindim, M., and Gaitonde, D. V., "Budget of Turbulent Kinetic Energy in a Shock Wave/Boundary-layer Interaction," *46th AIAA Fluid Dynamics Conference*, American Institute of Aeronautics and Astronautics, Washington, D.C., 2016. https://doi.org/10.2514/6.2016-3187, URL https://arc.aiaa.org/doi/10.2514/6.2016-3187.

[18] Mullenix, N., and Gaitonde, D., "Analysis of Unsteady Behavior in Shock/Turbulent Boundary Layer Interactions with Large-Eddy Simulations," *51st AIAA Aerospace Sciences Meeting Including the New Horizons Forum and Aerospace Exposition*, American Institute of Aeronautics and Astronautics, Grapevine (Dallas/Ft. Worth Region), Texas, 2013. https://doi.org/10.2514/6.2013-404, URL https://arc.aiaa.org/doi/10.2514/6.2013-404.

[19] Visbal, M., Rizzetta, D., and Mathew, J., "Large Eddy Simulation of Flow Past a 3-D Bump," *45th AIAA Aerospace Sciences Meeting and Exhibit*, American Institute of Aeronautics and Astronautics, Reno, Nevada, 2007. https://doi.org/10.2514/6.2007-917, URL https://arc.aiaa.org/doi/10.2514/6.2007-917.

[20] Poggie, J., Bisek, N. J., and Gosse, R., "Resolution Effects in Compressible, Turbulent Boundary Layer Simulations," *Computers & Fluids*, Vol. 120, 2015, pp. 57–69. https://doi.org/10.1016/j.compfluid.2015.07.015, URL https://linkinghub.elsevier.com/retrieve/pii/S0045793015002492.

[21] Mullenix, N. J., Gaitonde, D. V., and Visbal, M. R., "Spatially Developing Supersonic Turbulent Boundary Layer with a Body-Force-Based Method," *AIAA Journal*, Vol. 51, No. 8, 2013, p. 17. https://doi.org/10.2514/1.J051861.

[22] Pirozzoli, S., and Bernardini, M., "Turbulence in Supersonic Boundary Layers at Moderate Reynolds Number," *Journal of Fluid Mechanics*, Vol. 688, 2011, pp. 120–168. https://doi.org/10.1017/jfm.2011.368, URL https://www.cambridge.org/core/product/identifier/S0022112011003685/type/journal_article.

[23] Schwartz, M. J., and Garmann, D. J., "Investigation of Turbulent Inflow Techniques for High-Fidelity Simulations," *AIAA SCITECH 2023 Forum*, American Institute of Aeronautics and Astronautics, National Harbor, MD & Online, 2023. https://doi.org/10.2514/6.2023-2628, URL https://arc.aiaa.org/doi/10.2514/6.2023-2628.

[24] Van Driest, E. R., "The Problem of Aerodynamic Heating," *Aeronautical Engineering Review*, Vol. 15, 1956, pp. 26–41.

[25] Chapman, D. R., Kuehn, D. M., and Larson, H. K., "Investigation of Separated Flows in Supersonic and Subsonic Streams with Emphasis on the Effect of Transition," NACA Report 1356, NACA, Jan. 1958. URL https://ntrs.nasa.gov/citations/19930092343.

[26] Zheltovodov, A. A., and Yakovlev, V., "Stages of Development, Gas Dynamic Structures and Turbulence Characteristics of Turbulent Compressible Separated Flows in the Vicinity of 2-d Obstacles," *Preprint No. 27 Inst. Theor. Appl. Mech.,*, 1986.

[27] Hopkins, E. J., and Inouye, M., "An Evaluation of Theories for Predicting Turbulent Skin Friction and Heat Transfer on Flat Plates at Supersonic and Hypersonic Mach Numbers," *AIAA Journal*, Vol. 9, No. 6, 1971, pp. 993–1003. https://doi.org/10.2514/3.6323, URL https://arc.aiaa.org/doi/10.2514/3.6323.

[28] Gaitonde, D. V., and Adler, M. C., "Dynamics of Three-Dimensional Shock-Wave/Boundary-Layer Interactions," *Annual Review of Fluid Mechanics*, Vol. 55, No. 1, 2023, pp. 291–321. https://doi.org/10.1146/annurev-fluid-120720-022542, URL https://www.annualreviews.org/doi/10.1146/annurev-fluid-120720-022542.

[29] Visbal, M., and Gaitonde, D., "Shock Capturing Using Compact-Differencing-Based Methods," *43rd AIAA Aerospace Sciences Meeting and Exhibit*, American Institute of Aeronautics and Astronautics, Reno, Nevada, 2005. https://doi.org/10.2514/6.2005-1265, URL https://arc.aiaa.org/doi/10.2514/6.2005-1265.

[30] Welch, P., "The Use of Fast Fourier Transform for the Estimation of Power Spectra: A Method Based on Time Averaging over Short, Modified Periodograms," *IEEE Transactions on Audio and Electroacoustics*, Vol. 15, No. 2, 1967, pp. 70–73. https://doi.org/10.1109/TAU.1967.1161901, URL http://ieeexplore.ieee.org/document/1161901/.